

Leveraging Internal Viscous Flow to Extend the Capabilities of Beam-Shaped Soft Robotic Actuators

Yoav Matia, Tsah Elimelech, and Amir D. Gat

Abstract

Elastic deformation of beam-shaped structures due to embedded fluidic networks (EFNs) is mainly studied in the context of soft actuators and soft robotic applications. Currently, the effects of viscosity are not examined in such configurations. In this work, we introduce an internal viscous flow and present the extended range of actuation modes enabled by viscosity. We analyze the interaction between elastic deflection of a slender beam and viscous flow in a long serpentine channel embedded within the beam. The embedded network is positioned asymmetrically with regard to the neutral plane and thus pressure within the channel creates a local moment deforming the beam. Under assumptions of creeping flow and small deflections, we obtain a fourth-order integro-differential equation governing the time-dependent deflection field. This relation enables the design of complex time-varying deformation patterns of beams with EFNs. Leveraging viscosity allows to extend the capabilities of beam-shaped actuators such as creation of inertia-like standing and moving wave solutions in configurations with negligible inertia and limiting deformation to a small section of the actuator. The results are illustrated experimentally.

Keywords: viscous-elastic interaction, fluid structure interaction, soft actuators, soft robotics

Introduction

IN THIS WORK, we examine the interaction between a low-Reynolds-number flow in a serpentine channel network, embedded in a slender elastic beam, and the time-varying deflection field of the beam. The embedded fluidic network (denoted hereafter as EFN) is positioned asymmetrically to the neutral plane and thus pressurization of the channel network creates a local moment and deflection of the beam. The rate of change in the channel cross-section area affects the internal viscous flow, therefore connecting the flow-field to beam dynamics governed by the Euler–Bernoulli equation. The configuration and coordinate systems are illustrated in Figure 1.

The interaction between low-Reynolds-number flows and elastic deformation is relevant to various fields such as swimming of micro-organisms,¹ blood flow in small vesicles, viscous peeling,² and dynamics of elastocapillary coalescence,^{3,4} among other subjects.^{5–11} The configuration examined in this work is common to soft actuators^{12–19} and soft robotic applications,^{20–32} where current research is mostly focused on quasistatic solid dynamics and inviscid flows. Utilizing viscosity as studied in this work could provide an increased range of actuation modes available to a given actuator geometry.

The goal of this work is to examine low-Reynolds number fluid–structure interaction in the context of beam-like soft actuators driven by an embedded fluidic region. We show that viscous effects can be applied to significantly extend the possible deformation modes of such actuators. By connecting viscous dynamics to such a basic structural element, viscous actuation of more complex structures, comprising multiple beam elements, may be achieved (e.g., dynamic legged locomotion of a soft robot). In the Problem Formulation section, we formulate the problem configuration. In the Analysis section, we obtain a governing equation relating viscous flow to elastic deformation. In the Results section, we present several solutions of the governing equations, and in the Experimental Illustration section, these solutions are illustrated experimentally. The Concluding Remarks section includes a brief summary and some concluding remarks.

Problem Formulation

We consider the dynamics of an elastic beam, initially at rest, with a serpentine channel network embedded within it asymmetrically with regard to the neutral plane (Fig. 1a). The embedded channel network is filled with a viscous fluid and

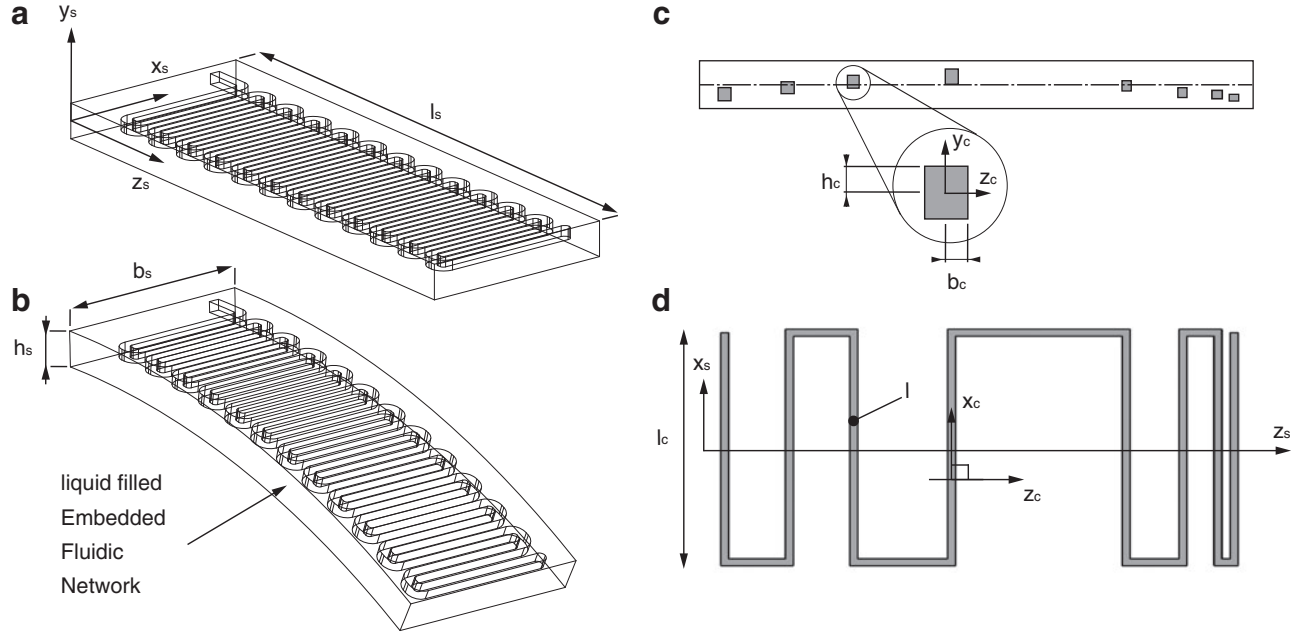


FIG. 1. An illustration of an interconnected parallel channel network positioned asymmetrically with respect to the neutral plane. **(a)** EFN at rest. **(b)** The deflection due to uniform pressure EFN. **(c)** $y_s - z_s$ plane and definition of channel cross section. **(d)** $x_s - z_s$ plane illustrating network with a varying channel density distribution. EFN, embedded fluidic network.

time-varying pressure is introduced at the channel inlets at one or both ends. Due to the pressure field applied by the fluid at the solid–fluid interface, the channel cross section deforms, thus deflecting the external beam structure (Fig. 1b).

We define beam height h_s , width b_s , and length l_s , and require $h_s/b_s \ll 1$ and $b_s/l_s \ll 1$. Young’s modulus, Poisson’s ratio, and mass per unit length of the beam are E , ν , and ρ_s , respectively. An interconnected parallel EFN is located within the beam perpendicular to the $x_s - y_s$ plane (Fig. 1a). The length of a single serpentine segment is denoted by l_c and the width of the beam by b_s , where $l_c/b_s \sim 1$. We limit our analysis to configurations with $l/l_c \gg 1$ and $(l_c \cdot n)/l \sim 1$, where l is the total length of the serpentine channel and n is the number of channel segments of length l_c , in order to allow approximating the discrete problem to a continuous function. The embedded channel network is assumed to be sufficiently small so as to have a negligible effect on the beam second moment inertia I and mass per unit length ρ_s .

The total deflection of the beam in the \hat{y}_s direction is denoted by d_s . Assuming small deflections, we can define $d_s = d_e + d_c$, where d_c is the deflection due to the embedded channel network and d_e is the additional deflection due to external forces and moments acting on the beam. We define the channel density of the parallel channel network as $\phi = 1/\delta z_s$, where δz_s is the distance between the centers of two adjacent channels. A single pressurized channel will create a change in beam slope, defined as ψ .¹⁴

The embedded channel coordinate system (x_c, y_c, z_c) is defined such that \hat{x}_c direction is the channel streamwise direction, h_c and b_c denote channel characteristic height in the \hat{y}_c direction and width in the \hat{z}_c direction, respectively. We assume $b_c \sim h_c$ and define a small parameter representing channel slenderness, $\varepsilon_1 = h_c/l \ll 1$. The parameters of the fluidic region are viscos-

ity, μ , velocity $u = (u, v, w)$, and gauge pressure, p . Channel cross-section area is defined as $a(x_c, p) = a_0(x_c) + a_1(x_c, p)$, where $a_0(x_c)$ is the cross-section area of the channel at gauge pressure $p = 0$, and $a_1(x_c, p)$ describes the change of the cross-section area due to the fluid pressure.

The governing equations for incompressible creeping Newtonian flow are the Stokes equation

$$\nabla p = \mu \nabla^2 u \quad (1)$$

and conservation of mass

$$\nabla \cdot u = 0. \quad (2)$$

In a previous work,¹⁴ we presented a modified Euler–Bernoulli equation governing the deflection of an EFN elastic beam,

$$\frac{\partial^2}{\partial z_s^2} \left[EI \left(\frac{\partial^2 d_s}{\partial z_s^2} + \phi(z_s) \frac{p(z_s, t)}{E} \frac{\partial \psi}{\partial (p/E)} \right) \right] = -\rho_s \frac{\partial^2 d_s}{\partial t^2} + f(z_s, t), \quad (3)$$

where $\phi(z_s)(p(z_s, t)/E) \partial \psi / \partial (p/E)$ represents the change in beam slope due to embedded network pressure and $f(z_s, t)$ is the external force per unit length applied to the beam surface. Equation (3) details a one-way coupling of fluid pressure to beam deflection and we thus limit our analysis to configurations where fluid pressure in the embedded network, created by external forces acting on the beam surface, is negligible compared with pressure applied at the network inlets.

We focus our analysis on parallel serpentine channel configurations embedded within a beam, as illustrated in

Figure 1d, and assuming $\phi(z_s) \gg 1$, the channel coordinate x_c may be related to the z_s beam coordinate through

$$x_c(z_s) = l_c \int_0^{z_s} \phi(z_s) dz_s + z_s. \quad (4)$$

Hereafter, we define normalized variables by capital letters and characteristic values by asterisk superscripts. We define the characteristic velocity (u^*, v^*, w^*), characteristic gauge pressure p^* , characteristic channel cross section at gage pressure a_0^* , characteristic change in channel cross section due to characteristic pressure a_1^* , viscous-elastic timescale t_f^* , characteristic channel density ϕ^* , characteristic total beam deflection d_s^* , characteristic elastic-inertial timescale t_s^* , and characteristic external force applied to the beam f^* .

We here define normalized variables and coordinates. These include normalized channel network spatial coordinates $(X_c, Y_c, Z_c) = (x_c/l, y_c/h_c, z_c/h_c)$, time $T = t/t_f^*$, fluid velocity (in the $[X_c, Y_c, Z_c]$ coordinates) $(U, V, W) = (u/u^*, v/v^*, w/w^*)$, pressure $P = p/p^*$, volume flow rate at channel cross section $Q = q/(h^2 u^*)$, channel density $\phi(Z_s) = \phi(z_s)/\phi^*$, beam spatial coordinates $(X_s, Y_s, Z_s) = (x_s/b_s, y_s/h_s, z_s/l_s)$ (Fig. 1c), beam total deflection $D_s = d_s/d_s^*$, and external forces applied to the beam $F = f/f^*$. Channel cross section $a(x_c, p) = a_0(x_c) + a_1(x_c, p)$ is normalized through a_0^* and a_1^* , such that it reads $A(X_c, P) = A_0(X_c) + \sigma_r \cdot A_1(P)$ where $\sigma_r = a_1^*/a_0^* = a_1^*/h^2$.

Methods

The manufacturing of the beam consists of a two-stage cast molding process. For the first stage, we used a 3D printed mold manufactured from FullCure[®] 720 using an Objet Eden250[™] printer, denoted hereafter as mold A. Liquid RTV silicone was poured into mold A. After curing, the silicone cast was used as the mold for the second stage, denoted mold B. Liquid polyurethane-based rubber was poured into mold B. To ensure geometric parallelism of cast faces, a glass pane and weights were set on top of the filled molds during the curing process in both stages. The molding process was used to separately create two halves of the beam, which were then glued together by a thin layer of the same polyurethane-based rubber. To create a strong adhesion, a glass pane and weights were set on the curing beam.

Beam Young's modulus E was estimated through a uniaxial stretching experiment on a sample piece of the polyurethane rubber. The beam property $\partial a_1/\partial p$, describing the change in channel cross-section area due to change in fluidic pressure, was calculated by applying known pressures at the channel inlet and measuring the displaced fluid volume. The experiment was repeated over various pressures and linear regression was used to obtain the value of $\partial a_1/\partial p$. Similarly, the coefficient $\partial \psi/\partial(p/E)$ was calculated by setting various pressures at the beam channel inlet and utilizing the Micro-Epsilon scanCONTROL 2650-100 laser profile sensor to measure the obtained deflections.

Analysis

Substituting the normalized parameters, we obtain

$$X_c = \int_0^{Z_s} \phi(Z_s) dZ_s + \frac{l_s}{l} \cdot Z_s, \quad (5)$$

and the resulting characteristic channel density $\phi^* = l/l_c l_s$. Substituting the normalized variables into Equations (1) and (2) yields, in leading order,

$$\frac{\partial P}{\partial X_c} \sim \frac{\partial^2 U}{\partial Y_c^2} + \frac{\partial^2 U}{\partial Z_c^2}, \quad \frac{\partial P}{\partial Y_c} \sim 0, \quad \frac{\partial P}{\partial Z_c} \sim 0, \quad (6)$$

$$\frac{\partial U}{\partial X_c} + \frac{\partial V}{\partial Y_c} + \frac{\partial W}{\partial Z_c} \sim 0 \quad (7)$$

where $h/l \sim v^*/u^* = \varepsilon_1 \ll 1$ and $u^* = p^* \varepsilon_1^2 / \mu$. Integrating Equation (7) over the channel cross section in the $Y_c - Z_c$ plane and applying Gauss theorem yields

$$\frac{\partial Q}{\partial X_c} + \frac{h}{t_f^* v^*} \frac{\partial A}{\partial T} = 0. \quad (8)$$

We define $Q_1(X, A(X_c, P))$ as the normalized volume flow rate calculated by the solution for the Poisson Equation (6); for $\partial P/\partial X_c = -1$ with no slip boundary conditions at the wall, $(U, V, W)|_{\text{wall}} = \underline{V}_{\text{wall}}$. From linearity, Q can be obtained from Q_1 by

$$Q = - \frac{\partial P}{\partial X_c} Q_1(A(X_c, P)). \quad (9)$$

Taking the derivative of $A(X_c, P) = A_0(X_c) + \sigma_r \cdot A_1(P)$ with regard to T and substituting Equation (9) into Equation (8) yields

$$- \left(\frac{\partial^2 P}{\partial X_c^2} \cdot Q_1(A(X_c, P)) + \frac{\partial P}{\partial X_c} \frac{\partial Q_1}{\partial X_c} \right) + \frac{\partial A_1(P)}{\partial P} \cdot \frac{\partial P}{\partial T} = 0, \quad (10)$$

where order-of-magnitude analysis of Equation (10) determines the viscous-elastic timescale t_f^* as

$$t_f^* = \frac{\sigma_r \mu}{p^* \varepsilon_1^2} = \frac{a_1^* \mu}{a_0^* p^* \varepsilon_1^2}. \quad (11)$$

The resulting convection–diffusion equation may be nonlinear due to the pressure-dependent coefficients $Q_1(A(X_c, P))$ and $\partial A_1(P)/\partial P$, which govern the diffusivity coefficient. Setting both to constants degenerates Equation (10) to a linear diffusion equation without the transport term (of the form $\partial P/\partial T = Q_1 \partial^2 P/\partial X_c^2$) and the characteristic timescale becomes $t_f^* = \mu(\partial a_1/\partial p)|_{p=p_0}/a_0^* \varepsilon_1^2$.

Substituting the normalized variables into Equation (3), we get

$$\frac{\partial^2}{\partial Z_s^2} \left[\left(\frac{\partial^2 D_s}{\partial Z_s^2} + \Phi(Z_s) \cdot P(X_c, T) \frac{\partial \psi}{\partial(p/E)} \right) \right] = - \frac{\partial^2 D_s}{\partial T^2} \cdot \left(\frac{t_s^*}{t_f^*} \right)^2 + F(Z_s, T), \quad (12)$$

with order-of-magnitude analysis yielding

$$d_s^* = \frac{l_s^2 \phi^* \mu u^*}{E e_1^2 l} \quad (13)$$

and

$$f^* = \frac{\phi^* P^* I}{l_s^2}, \quad (14)$$

where the elastic-inertial timescale is $t_s^* = \sqrt{\rho_s l_s^4 / EI}$.

We define the ratio $\lambda = t_s^* / t_f^*$, which determines the relevant regime of beam dynamics. For the limit of small deformations and constant coefficients $Q_1(A(X_c, P))$ and $\partial A_1(P) / \partial P$, the value of λ is given by

$$\lambda = \frac{t_s^*}{t_f^*} = \frac{\sqrt{\rho_s l_s^4 / EI} a_0^* e_1^2}{\mu (\partial a_1 / \partial p)|_{p=p_0}}. \quad (15)$$

For $\lambda \gg 1$, the viscous–elastic interaction propagates significantly faster than inertial beam response, and the beam behaves as responding to a spatially uniform time-varying pressure. This case was studied in a previous work.¹⁴ For $\lambda = O(1)$, the spatial pressure variation within the network must be accounted for in the analysis and solid inertia will take part in the interaction. For $\lambda \ll 1$, beam inertia is negligible and the beam deflection reflects viscous-elastic dynamics within the EFN.

Rewriting Equation (12) to isolate $P(Z_s, T)$ and applying coordinate transformation Equations (5) to (10) yields the governing equation system for the beam deflection,

$$P(Z_s, T) = \left(\Phi(Z_s) \frac{\partial \psi}{\partial (p/E)} \right)^{-1} \left(\int_0^{Z_s} \int_0^\zeta \left(F(\eta, T) - \frac{\partial^2 D_s}{\partial T^2} \lambda^2 \right) d\eta d\zeta - \frac{\partial^2 D_s}{\partial Z_s^2} \right) \quad (16)$$

$$\left(\phi(Z_s) + \frac{l_s}{l} \right)^{-1} \frac{\partial}{\partial Z_s} \left(\left(\phi(Z_s) + \frac{l_s}{l} \right)^{-1} \frac{\partial P}{\partial Z_s} \right) Q_1 + \left(\phi(Z_s) + \frac{l_s}{l} \right)^{-2} \frac{\partial P}{\partial Z_s} \frac{\partial Q_1}{\partial Z_s} = \frac{\partial A_1(P)}{\partial P} \frac{\partial P}{\partial T}. \quad (17)$$

Substituting Equation (16) into Equation (17), we obtain the general form governing equation for beam deflection as a fourth-order partial nonlinear integro-differential equation. Choosing spatially uniform channel cross section, the parameters $\partial \psi / \partial (p/E)$, $\partial A_1(P) / \partial P$, and $Q_1(A(Z_s, P))$ become constants for sufficiently small deformation of the channel cross section. Setting the network density $\Phi(Z_s)$ to constant as well, Equations (16) and (17) may be combined to a simplified governing equation of the form

$$\left(\frac{l_s}{l} + \Phi \right)^2 \frac{\partial A_1}{\partial P} \left[\int_0^{Z_s} \int_0^\zeta \left(\frac{\partial F(\eta, T)}{\partial T} - \frac{\partial^3 D_s}{\partial T^3} \lambda^2 \right) d\eta d\zeta - \frac{\partial^3 D_s}{\partial Z_s^2 \partial T} \right] + Q_1 \left[\left(F(Z_s, T) - \frac{\partial^2 D_s}{\partial T^2} \lambda^2 \right) - \frac{\partial^4 D_s}{\partial Z_s^4} \right] = 0. \quad (18)$$

The parameter $\partial \psi / \partial (p/E)$, which scales deflection, now appears only in the boundary and initial conditions.

Equation (18) requires four boundary conditions and three initial conditions. First, we define F_i as the boundary or initial condition function. Next, we define four possible boundary conditions over D_s , formulated as a set of geometric and dynamic conditions. Geometric conditions over deflection

$$D_s(\alpha, T) = F_1(T) \quad (19)$$

or slope

$$\left(\frac{\partial D_s}{\partial Z_s} \right) \Big|_{(\alpha, T)} = F_2(T), \quad (20)$$

remain unchanged compared with standard Euler–Bernoulli boundary conditions since they are applied directly on the total deformation of the beam D_s . The deflection due to EFN actuation in the absence of external forces and moments is denoted by D_c , which is related to P through [see Ref.¹⁴, eq. (4)]

$$\frac{\partial^2 D_c}{\partial Z_s^2} = -\Phi(Z_s) \cdot P(Z_s, T) \frac{\partial \psi}{\partial (p/E)}. \quad (21)$$

External forces or moments acting on the EFN-actuated beam will create an additional deflection denoted as D_e . Since the total deflection is $D_s = D_c + D_e$, we apply Equation (21) to relate the additional deflection due to moments and shear forces at the boundaries to the total deflection D_s . This yields the moment boundary condition

$$\left(\frac{\partial^2 D_s}{\partial Z_s^2} \right) \Big|_{(\alpha, T)} = F_3(T) - \Phi(Z_s) \cdot P(\alpha, T) \frac{\partial \psi}{\partial (p/E)} \quad (22)$$

and the shear force boundary condition

$$\left(\frac{\partial^3 D_s}{\partial Z_s^3} \right) \Big|_{(\alpha, T)} = F_4(T) - \frac{\partial}{\partial Z_s} \left(\Phi(Z_s) \cdot P(\alpha, T) \frac{\partial \psi}{\partial (p/E)} \right), \quad (23)$$

where the moment is $M = F_3(T)$, the shear force is $V = F_4(T)$, and $P(\alpha, T)$ is the applied pressure set at $\alpha = 0$ or

$\alpha = 1$. The initial conditions of the deflections are directly given by

$$D_s(Z_s, 0) = F_5(Z_s), \quad (24)$$

$$\left. \left(\frac{\partial D_s}{\partial T} \right) \right|_{(Z_s, 0)} = F_6(Z_s) \quad (25)$$

which are supplemented by the initial condition of the pressure distribution within the channel

$$P(Z_s, 0) = F_7(Z_s). \quad (26)$$

Results

Figures 2–5 present several solutions of Equation (18), illustrating the viscous-elastic dynamics of a beam with an EFN, actuated by a time-varying pressure at the inlets. In all presented cases, the beam and channel network are of identical geometry and physical properties. We set the timescale ratio as $\lambda = t_s^*/t_f^* \ll 1$, thus solid inertia is negligible. We focus on small deformations and therefore set $\partial A_1(P)/\partial P = 1$,

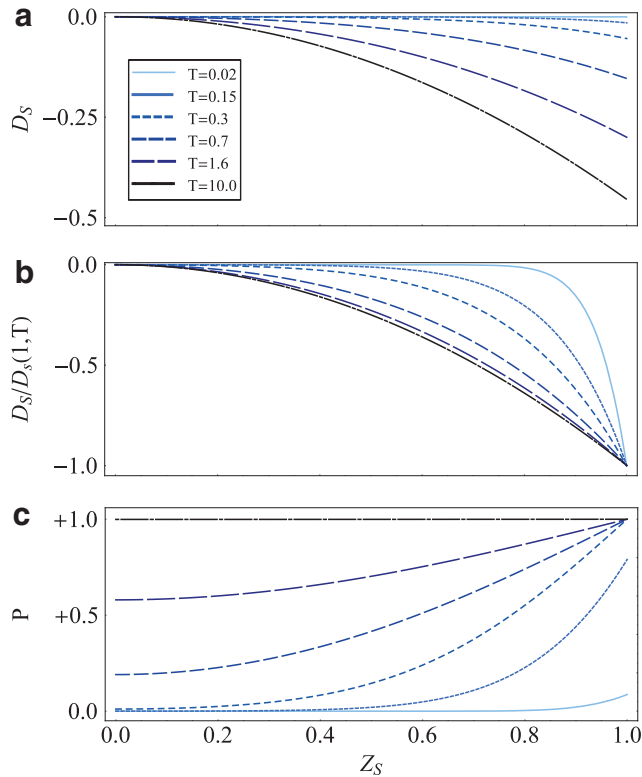


FIG. 2. Cantilever EFN beam with a suddenly applied inlet pressure. Cantilever beam clamped at $Z_s = 0$, starting from rest $D_s(Z_s, T \leq 0) = 0$, with boundary conditions of ramp pressure $P(Z_s = 1, T) = H(T)$, where $H(T)$ is the Heaviside function and $\partial P/\partial Z_s(Z_s = 0) = 0$. **(a)** Beam deflection, **(b)** beam deflection normalized by $D_s(1, T)$, **(c)** pressure. All plots are presented versus Z_s for various times, $T = 0.02, 0.15, 0.3, 0.7, 1.6$, and 10 . Color images available online at www.liebertpub.com/soro

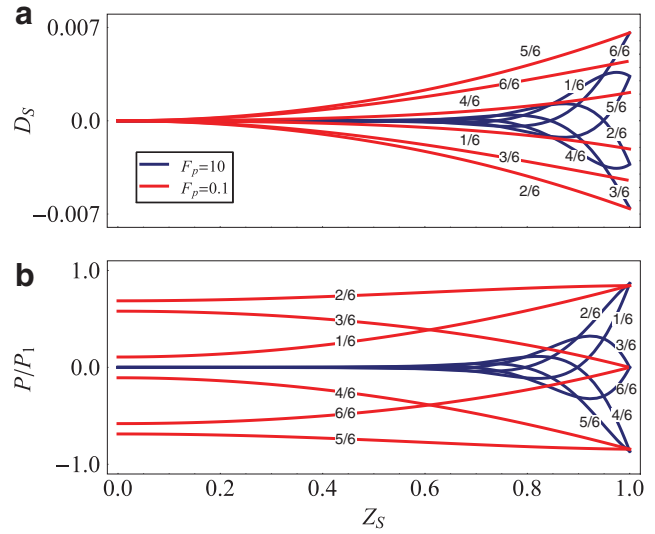


FIG. 3. Cantilever EFN beam with an oscillating inlet pressure. Cantilever beam with an oscillating pressure inlet introduced at $Z_s = 1$ as $P(1, T) = P_1 \sin(2\pi F_p \cdot T)$ setting $F_p = 10$ and $P_1 = 1.3$ (solid blue) and $F_p = 0.1$ and $P_1 = 0.02$ (solid red). Plotted lines represent a single cycle period divided into six equal parts marked with respective plot line labels. Deflection **(a)** and pressure **(b)** are presented versus Z_s . Color images available online at www.liebertpub.com/soro

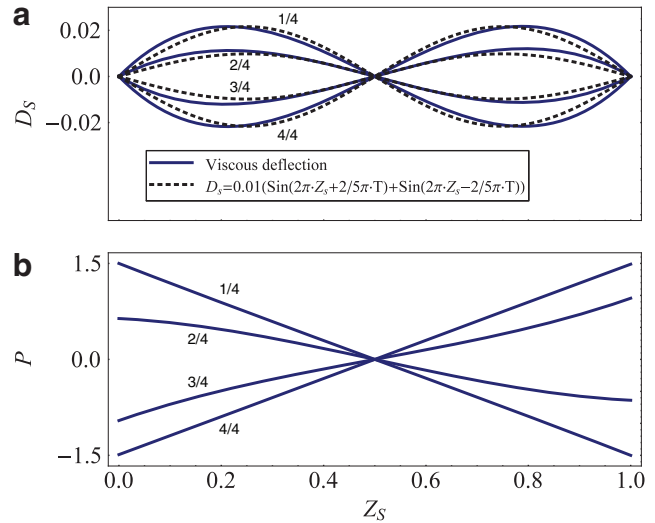


FIG. 4. Simply supported beam with an oscillating pressure introduced at both ends, producing a standing wave. Simply supported beam with an oscillating pressure introduced to inlets at both ends, defined by $P(0, T) = 1.5 \sin(2\pi T/5 + \pi/2)$ and $P(1, T) = 1.5 \sin(2\pi T/5 + 3\pi/2)$. Plotted lines represent a single cycle period divided into four equal parts marked with respective plot line labels. **(a)** Viscous deflection (solid blue lines) and exact standing wave $D_s(Z_s, T) = 0.01(\sin(2\pi Z_s + 2\pi T/5) + \sin(2\pi Z_s - 2\pi T/5))$, (dashed black lines) versus Z_s . **(b)** Respective pressure profiles along beam length. Color images available online at www.liebertpub.com/soro

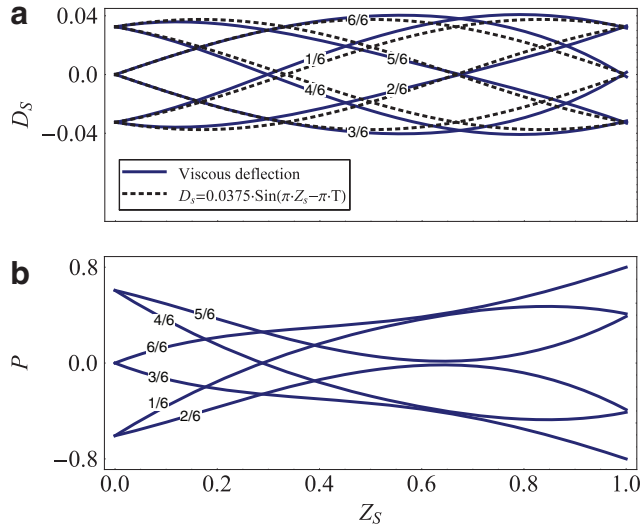


FIG. 5. Beam with an oscillating pressure introduced at both ends, producing a moving wave. Beam support at $Z_s = 0$ is externally excited by $(D_s)|_{(0,T)} = -0.0375 \sin(\pi T)$ and $(\partial D_s / \partial Z_s)|_{(0,T)} = \pi \cdot 0.0375 \cos(\pi T)$, free at $Z_s = 1$. Oscillating pressure is introduced to inlets at both ends $P(0, T) = 0.7 \sin(\pi T + \pi)$ and $P(1, T) = 0.8 \sin(\pi T + \pi/2)$. Plotted lines represent a single cycle period divided into six equal parts marked with respective plot line labels. **(a)** Deformation due to viscous-elastic dynamics (solid blue lines) and an exact moving wave, $D_s(Z_s, T) = 0.0375 \sin(\pi Z_s - \pi T)$, (dashed black lines) versus Z_s . **(b)** Respective pressure profiles along beam length. Color images available online at www.liebertpub.com/soro

$Q_1(A(Z_s, P)) = 0.3$, and $\partial \psi / \partial (p/E) = 1$ to constants. In addition, in all cases, we examine a uniform channel distribution $\phi(Z_s) = 1$.

Figure 2 illustrates a suddenly applied inlet pressure, propagating through diffusion down the length of the channel. The examined configuration is a cantilever beam, clamped at $Z_s = 0$, starting from rest $D_s(Z_s, T \leq 0) = 0$. A ramp pressure boundary condition $P(Z_s = 1, T) = H(T)$ is introduced, where $H(T)$ is the Heaviside function, and the channel is sealed at $Z_s = 0$, $\partial P / \partial Z_s(Z_s = 0) = 0$. Beam deflection D_s (Fig. 2a), scaled beam deflection $D_s/D_s(1, T)$ (Fig. 2b), and fluid pressure P (Fig. 2c) are presented versus Z_s for various times, $T = 0.02, 0.15, 0.3, 0.7, 1.6$, and 10 . Both the pressure and deformation fields propagate into the beam with speed of order of magnitude of $O(1)$ [in dimensional terms, $O(l a_0^* e_1^2 / \mu (\partial a_1 / \partial p)|_{p=p_0})$]. For $T \ll 1$, the viscous-elastic dynamics have yet to propagate throughout the length of the channel and only a part of the beam is deflected. Thus, the boundary condition imposed on the pressure at $Z_s = 0$ does not affect the dynamics until $T \approx 0.3$, where pressure at the clamped end starts to build. For $T = O(1)$, the entire length of the beam has been engaged and pressure slowly builds along its length until achieving steady state.

Following Figure 2, introducing an oscillating pressure with a significantly smaller oscillation period compared with the viscous-elastic timescale, we expect only part of the beam to deflect. In Figure 3, we examine such a cantilever beam where the inlet pressure at $Z_s = 1$ is $P(1, T) = P_1 \sin(2\pi F_p \cdot T)$. All

other boundary conditions are identical to the beam in Figure 2. Varying the inlet frequency $F_p = f[Hz] \cdot t_f^*[s]$ and the amplitude of pressure oscillations P_1 , we are able to control the length of the beam engaged in the oscillating motion. Setting $F_p = 0.1$ and $P_1 = 0.02$ creates a beam deflection of $D_s \approx 0.006$ at $Z_s = 1$, where the entire beam is engaged (marked in solid red lines). Setting $F_p = 10$ and $P_1 = 1.5$, we are able to produce an identical beam deflection at $Z_s = 1$, only this time limiting the engaged beam length to $0.6 \leq Z_s \leq 1$ (marked in solid blue). Plotted lines represent a single cycle period divided into six equal parts marked with respective plot line labels.

In Figures 4 and 5, we illustrate the application of an oscillating pressure introduced to inlets at both ends as a mechanism to create wave-like deflection fields. Matching frequency and amplitude while modifying the phase, we are able to create standing and moving waves in a system without inertia, through viscous effects alone.

In Figure 4, we illustrate the deflection D_s (Fig. 4a) and pressure P (Fig. 4b) versus Z_s for a simply supported beam, hinged at $Z_s = 0$ and $Z_s = 1$. Pressure is applied at both ends, defined by $P(0, T) = 1.5 \sin(2\pi \cdot 0.2T + \pi/2)$ and $P(1, T) = 1.5 \sin(2\pi \cdot 0.2T + 3\pi/2)$. The obtained viscous-elastic deformation field (solid blue lines) closely follows an inertial standing wave of the form $D_s(Z_s, T) = 0.01(\sin(2\pi Z_s + 2\pi \cdot 0.2 \cdot T) + \sin(2\pi Z_s - 2\pi \cdot 0.2 \cdot T))$, (dashed black lines). Plotted lines represent a single cycle period divided into four equal parts marked with respective plot line labels.

In Figure 5, the beam support at $Z_s = 0$ oscillates with $(D_s)|_{(0,T)} = -0.0375 \sin(\pi T)$ and $(\partial D_s / \partial Z_s)|_{(0,T)} = \pi \cdot 0.0375 \cos(\pi T)$. The beam is free at $Z_s = 1$ and pressure is introduced to inlets at both ends by $P(0, T) = 0.7 \sin(\pi T + \pi)$ and $P(1, T) = 0.8 \sin(\pi T + \pi/2)$. In this case, the deformation of the beam (blue solid line) closely matches an exact moving wave given by $D_s(Z_s, T) = 0.0375 \sin(\pi Z_s - \pi T)$ (dashed black lines). Plotted lines represent a single cycle period divided into six equal parts marked with respective plot line labels.

Experimental Illustration

An EFN beam was fabricated, with the following beam parameters: $h_s = 12$ [mm], $l_s = 200$ [mm], $b_s = 90$ [mm], $l_c = 56$ [mm], $l = 1600$ [mm], $h_c = 2$ [mm], $b_c = 2$ [mm] and embedded with a total of $n = 25$ channels. To apply pressure to the EFN at the beam free end without affecting beam dynamics, two auxiliary channels were added. The channels connect the EFN far end to an inlet at the clamped end. The channels were positioned symmetrically with regard to the neutral plane and have a circular cross section with a diameter of 4 [mm].

The EFN beam structural properties are measured to be $\partial \psi / \partial (p/E) \approx 0.4$ and $\partial a_1^* / \partial p \approx 8.75 \cdot 10^{-11}$ [m²/Pa]. The experimental setup is illustrated in Figure 6. In all experiments, the beam was positioned with its deflection plane perpendicular to gravity, acting in the X_s direction. Deformation was measured relative to the contour of the beam at rest, and the beam was allowed to achieve equilibrium between experiments over a period of time no less than one order of magnitude greater than the viscous-elastic timescale. Using Elveflow[®] OB1 MK3 pressure controller to pressurize a fluid reservoir connected to the EFN, we introduced a varying pressure signal at the channel inlets and measured the beam deflection by a MicroEpsilon scanCONTROL 2650-100 laser

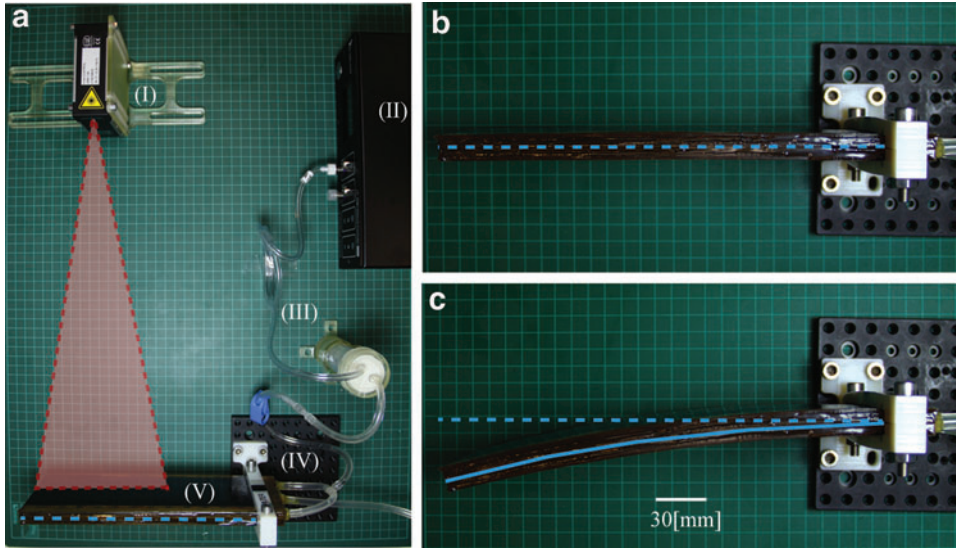


FIG. 6. Illustration of experimental setup. (a) Setup components (I) scanCONTROL 2650-100 laser profile, (II) Elveflow[®] OB1 MK3 pressure controller, (III) fluid reservoir, (IV) beam stand, and (V) EFN beam. (b) EFN beam at rest. (c) Actuated EFN beam. *Solid blue line* represents neutral plane at steady state of the actuated beam. Beam neutral plane at rest is illustrated in *dashed blue line* and laser field in transparent *red*. Color images available online at www.liebertpub.com/soro

profile sensor. The sensor was positioned 330[mm] from the beam and was able to measure a region of $0.4 \leq Z_s \leq 1$ of the beam length, providing 640 spatial sample points.

Beam material is a two-component polyurethane-based rubber. Material Young's modulus was measured using Hooke's law and recording the elongation of a rectangular sample loaded with known weights, $E \approx 1.5$ [MPa]. Density was calculated through sample weight-to-volume ratio, $\rho \approx 1110$ [Kg/m³]. In all experiments, we first initiated the laser scanner and immediately activated the Elveflow pressure controller, setting $t=0$ to be the time when deflection was first noted by the laser scanner. Beam deformation was kept at least one order of magnitude less than beam length, $d_s/l_s \ll 1$, thus ensuring solid strain field in the elastic limit. All experimental results shown after applying a moving average of 50 sample points over 5 consecutive experiments and error bars represent one standard deviation.

To clearly illustrate the diffusive propagation of beam deflection, we applied a sudden pressure of the form $p(t \geq 0^+, z_s = l_s) = 101$ [KPa] at the free end of the beam

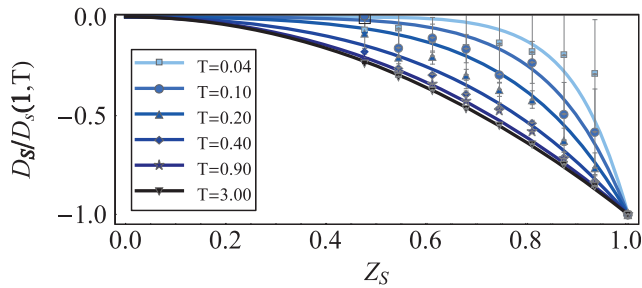


FIG. 7. Experimental data of a cantilever EFN beam with a suddenly applied inlet pressure. Cantilever beam with $Z_s = 0$ set at beam clamp, starting from rest $D_s(Z_s, T \leq 0) = 0$, with boundary conditions of step pressure $P(Z_s = 1, T) = H(T)$, where $H(T)$ is the Heaviside function and $\partial P / \partial Z_s(Z_s = 0) = 0$. Beam deflection normalized by $D_s(1, T)$ is presented versus Z_s , comparing theoretical prediction (*solid lines*) with experimental data (*markers*). Error bars denote one standard deviation. Color images available online at www.liebertpub.com/soro

and blocked the inlet at the clamped end at $z_s = 0$. The channel network was filled with a high viscosity silicone oil, $\mu = 58.2$ [Pa · s]. Figure 7 presents beam deflection normalized by $D_s(1, T)$ versus Z_s for several normalized times (tip deflection at $T = 3$ was $d_s \approx 30.6$ [mm], and $p^* = 101$ [KPa]). Theoretical solutions of Equation (18) are presented by solid

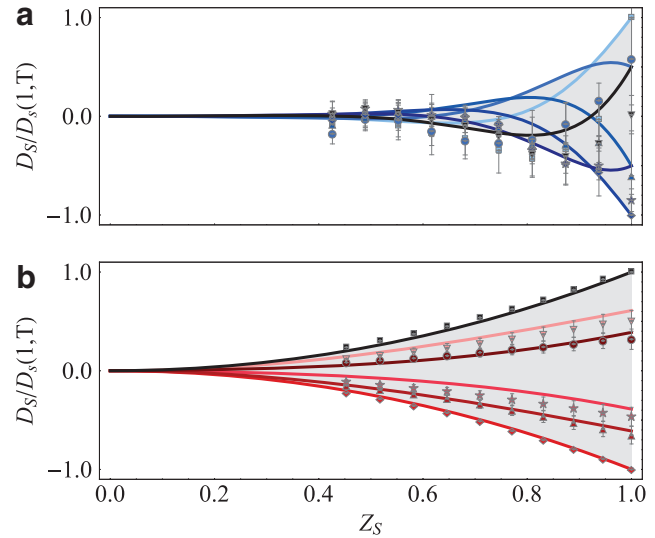


FIG. 8. Experimental data of a cantilever EFN beam with oscillating inlet pressure. Cantilever beam starting from rest with an oscillating pressure inlet introduced at $Z_s = 1$ as $P(1, T) = P_1 \sin(2\pi F_p \cdot T)$, where $P_1 = p_1/p^*$, $p_1 = 70$ [KPa], and $f = 0.01$ [Hz]. (a) Silicone oil-actuated EFN beam $\mu = 58.2$ [Pa · s], $t_f^* \approx 814$ [s], normalized frequency of $F_p \approx 8.14$, and resulting $d_s \approx 0.066$ [mm]. (b) Glycerol-actuated EFN beam $\mu = 1.15$ [Pa · s], $t_f^* \approx 16.1$ [s], normalized frequency of $F_p \approx 0.16$, and resulting $d_s \approx 19.6$ [mm]. Deflection is illustrated through centerline and each cycle is divided into six equal parts. Cycle progresses with time from light to dark. Beam deflection is normalized by $D_s(1, T)$ versus Z_s , comparing theoretical prediction (*lines*) with experimental results (plot markers with error bars). Color images available online at www.liebertpub.com/soro

lines and experimental results are denoted by markers. The experimental data clearly depict concentration of the deformation to the region near $z_s \approx l_s$ for early normalized times $T \ll 1$, in agreement with the analytic results.

To illustrate the effects of fluid viscosity on beam response to oscillating inlet pressure, we set two identical beams actuated through an identical inlet signal, $P(1, T) = P_1 \sin(2\pi F_p \cdot T)$, introduced at $Z_s = 1$, where $P_1 = p_1/p^*$, setting $p_1 = 70$ [KPa] and $f = 0.01$ [Hz]. Figure 8a presents a silicone oil-filled EFN beam, $\mu \approx 58.2$ [Pa · s], $t_f^* \approx 814$ [s], normalized frequency of $F_p \approx 8.14$, and resulting $d_s \approx 0.066$ [mm]. Figure 8b shows a glycerol-actuated EFN beam, $\mu \approx 1.15$ [Pa · s], $t_f^* \approx 16.1$ [s], normalized frequency of $F_p \approx 0.16$, and resulting $d_s \approx 19.6$ [mm]. Good agreement of experimental data and theoretical prediction is evident.

Concluding Remarks

In this work, we examined the effect of viscosity on the possible deformation fields of beam-shaped soft actuators driven by embedded pressurized fluid. We showed analytically and experimentally that by setting appropriate time-varying inlet pressure signal, viscosity enables to increase the possible deformation patterns available to a given actuator geometry. These include limiting the deformation to a section of the actuator as well as creating inertia-like waves in an inertialess configuration. The presented model can be readily expanded to more complex structures by superimposing several beams in parallel or series.

Applying viscous effects to common soft robotic configurations (comprising materials such as PDMS or silicone and with characteristic length scale of 1 [cm]) requires introduction of a sufficiently viscous-driving fluid such as glycerin ($\mu \approx 1$ Pa · s) to have similar viscous-elastic and elastic-inertial timescales. Alternatively, similar timescales may occur for low-viscosity fluids due to miniaturization of soft robots and soft actuators.³³

Our analysis focused on configurations where the effect of externally applied bending moment on the pressure within the channel network is negligible compared with the pressure applied at the networks' inlets. While this is a reasonable assumption for beams actuated through a pressurized channel network, the effect of a closed EFN on the dynamic response of the beam to external forces is not modeled in this work and may be of interest in a future study. In addition, while the current analysis utilized the lubrication approximation for the channel flow field coupled with Euler–Bernoulli model for the solid, poroelastic mixture models could be leveraged to examine similar configurations in future works involving porous structures.

Acknowledgments

This research is funded by Israel, Ministry of Science, Technology and Space. The authors thank the Israel Science Foundation (Grant No. 818/13) for their contribution in funding this research.

Authors' Contributions

Y.M. and A.D.G. jointly conceived the study, created the analytic model, developed analytical tools, analyzed data, and wrote the article; Y.M. designed and implemented the

simulation model; T.E. and A.D.G. performed experiments and collected and analyzed data; and A.D.G. supervised the project and manuscript.

Author Disclosure Statement

No competing financial interests exist.

References

1. Lauga E, Powers TR. The hydrodynamics of swimming microorganisms. *Rep Prog Phys* 2009;72:096601.
2. Lister JR, Peng GG, Neufeld JA. Viscous control of peeling an elastic sheet by bending and pulling. *Phys Rev Lett* 2013;111:154501.
3. Gat AD, Gharib M. Elasto-capillary coalescence of multiple parallel sheets. *J Fluid Mech* 2013;723:692–705.
4. Singh K, Lister JR, Vella D. A fluid-mechanical model of elastocapillary coalescence. *J Fluid Mech* 2014;745:621–646.
5. Canic S, Mikelic A. Effective equations modeling the flow of a viscous incompressible fluid through a long elastic tube arising in the study of blood flow through small arteries. *SIAM J Appl Dyn Syst* 2003;2:431–463.
6. Duprat C, Stone HA. (Eds). *Fluid-Structure Interactions in Low-Reynolds-Number Flows*. Cambridge, UK: Royal Society of Chemistry, 2015.
7. Elbaz SB, Gat AD. Dynamics of viscous liquid within a closed elastic cylinder subject to external forces with application to soft robotics. *J Fluid Mech* 2014;758:221–237.
8. Heil M, Pedley TJ. Large axisymmetric deformation of a cylindrical shell conveying a viscous flow. *J Fluids Struct* 1995;9:237–256.
9. Ku DN. Blood flow in arteries. *Annu Rev Fluid Mech* 1997;29:399–434.
10. Paidoussis MP. *Fluid-Structure Interactions: Slender Structures and Axial Flow*, vol. 1. London, UK: Academic Press, 1998.
11. Cederbaum G, LePing L, Kalman S. (Eds). *Poroelastic Structures*. Amsterdam, Netherlands: Elsevier, 2000.
12. Chakraborty D, Prakash JR, Friend J, Yeo L. Fluid-structure interaction in deformable microchannels. *Phys Fluids* 2012;24:102002.
13. Chang BCM, Berring J, Venkataram M, Menon C, Parameswaran M. Bending fluidic actuator for smart structures. *Smart Mater Struct* 2011;20:035012.
14. Matia Y, Gat AD. Dynamics of elastic beams with embedded fluid-filled parallel-channel networks. *Soft Robot* 2015;2:42–47.
15. Pihler-Puzović D, Illien P, Heil M, Juel A. Suppression of complex fingerlike patterns at the interface between air and a viscous fluid by elastic membranes. *Phys Rev Lett* 2012;108:074502.
16. Polygerinos P, Lyne S, Wang Z, *et al.* Towards a soft pneumatic glove for hand rehabilitation. In: 2013 IEEE/RSJ International Conference on Intelligent Robots and Systems (IROS). IEEE, 2013, pp. 1512–1517.
17. Shapiro Y, Wolf A, Gabor K. Bi-bellows: pneumatic bending actuator. *Sensors Actuat A Phys* 2011;167:484–494.
18. Tezduyar TE, Sathe S. Modelling of fluid–structure interactions with the space–time finite elements: solution techniques. *Int J Numer Meth Fluids* 2007;54:855–900.
19. de Payrebrune KM, O'Reilly OM. On constitutive relations for a rod-based model of a pneu-net bending actuator. *Extreme Mech Lett* 2016;38–46.

20. Tolley MT, Shepherd RF, Mosadegh B, *et al.* A resilient, untethered soft robot. *Soft Robot* 2014;1:213–223.
21. Ilievski F, Mazzeo AD, Shepherd RF, Chen X, Whitesides GM. Soft robotics for chemists. *Angew Chem Int Ed Engl* 2011;50:1890–1895.
22. Katzschmann RK, Marchese AD, Rus D. Hydraulic autonomous soft robotic fish for 3D swimming. In: *International Symposium on Experimental Robotics (ISER)*. Marrakech, Morocco, 2014.
23. Laschi C, Mazzolai B, Mattoli V, Cianchetti M, Dario P. Design of a biomimetic robotic octopus arm. *Bioinspir Biomim* 2009;4:015006.
24. Luo M, Tao W, Chen F, Khoo TK, Ozel S, Onal CD. Design improvements and dynamic characterization on fluidic elastomer actuators for a soft robotic snake. In: *2014 IEEE International Conference on Technologies for Practical Robot Applications (TePRA)*. IEEE, 2014, pp. 1–6.
25. MacCurdy R, *et al.* Printable hydraulics: a method for fabricating robots by 3D co-printing solids and liquids. *arXiv Preprint 2015;arXiv:1512.03744*.
26. Majidi C. Soft robotics: a perspective—current trends and prospects for the future. *Soft Robot* 2014;1:5–11.
27. Marchese AD, Onal CD, Rus D. Autonomous soft robotic fish capable of escape maneuvers using fluidic elastomer actuators. *Soft Robot* 2014;1:75–87.
28. Marchese AD, Katzschmann RK, Rus D. A recipe for soft fluidic elastomer robots. *Soft Robot* 2015;2:7–25.
29. Morin SA, Kwok SW, Lessing J, *et al.* Elastomeric tiles for the fabrication of inflatable structures. *Adv Funct Mater* 2014;24:5541–5549.
30. Mosadegh B, Polygerinos P, Keplinger C, *et al.* Pneumatic networks for soft robotics that actuate rapidly. *Adv Funct Mater* 2014;24:2163–2170.
31. Onal CD, Chen X, Whitesides GM, Rus D. Soft mobile robots with on-board chemical pressure generation. In: *International Symposium on Robotics Research*. Switzerland: Springer International Publishing 2011, pp. 1–16.
32. Onal CD, Rus D. A modular approach to soft robots. In: *2012 Fourth IEEE RAS and EMBS International Conference on Biomedical Robotics and Biomechanics (BioRob)*. IEEE, pp. 1038–1045.
33. Paek J, Cho I, Kim J. Microrobotic tentacles with spiral bending capability based on shape-engineered elastomeric microtubes. *Sci Rep* 2015;5:10768.

Address correspondence to:

*Yoav Matia
Faculty of Mechanical Engineering
Technion–Israel Institute of Technology
Technion City
Haifa 3200003
Israel*

E-mail: yoavm@tx.technion.ac.il